# Luminescence Saturation via Mn²⁺−Exciton Cross Relaxation in Colloidal Doped Semiconductor Nanocrystals

Liam R. Bradshaw, Andreas Hauser,[†] Emily J. McLaurin, and Daniel R. Gamelin*

Department of Chemistry, University of Washington, Seattle, Washington 98195-1700, United States

Ⓢ *Supporting Information*

**ABSTRACT:** Colloidal Mn²⁺-doped semiconductor nanocrystals such as Mn²⁺:ZnSe have attracted broad attention for potential applications in phosphor and imaging technologies. Here, we report saturation of the sensitized Mn²⁺ photoluminescence intensity at very low continuous-wave (CW) and quasi-CW photoexcitation powers under conditions that are relevant to many of the proposed applications. Time-resolved photoluminescence measurements and kinetic modeling indicate that this saturation arises from an Auger-type nonradiative cross relaxation between an excited Mn²⁺ ion and an exciton within the same nanocrystal. A lower limit of $k = 2 \times 10^{10}$ s⁻¹ is established for the fundamental rate constant of the Mn²⁺($^4T_1$)-exciton cross relaxation.
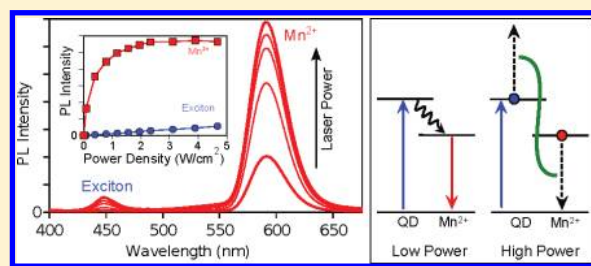
## I. INTRODUCTION

Mn²⁺ is an effective luminescence activator in many semiconductor matrices, and consequently Mn²⁺-doped semiconductors have been employed as phosphors in photoluminescent and electroluminescent technologies for many years.[1−3] In photoluminescence (PL), photoexcitation of the semiconductor is followed by rapid (picosecond) nonradiative energy transfer to excite Mn²⁺ to its $^4T_1$ state (Mn*), which then relaxes back to the $^6A_1$ ground state radiatively with approximately millisecond lifetimes, depending on the lattice and temperature.[4−8] The long Mn²⁺ $^4T_1$ excited-state lifetime is a bottleneck at large excitation rates, however, causing luminescence saturation.[9−11] In bulk Mn²⁺-doped semiconductors, a combination of Mn²⁺ concentration-dependence and PL time-dependence measurements has led to the conclusion that saturation is not only associated with depletion of ground-state Mn²⁺ but also depends on Mn* energy migration and nonradiative Mn*−Mn* cross relaxation.[11−15] In electroluminescent devices, Mn*−electron Auger-type de-excitation has also been identified as an important deactivation mechanism.[12,16−19]

Considerable recent effort has turned to doping semiconductor nanostructures with Mn²⁺. Exploration of these classic phosphor materials on nanometer length scales has uncovered completely new physical properties,[8,20−22] the technological potential of which cannot be fully assessed until the properties themselves are understood at a fundamental level. For example, the ability to detect and manipulate individual spins has been demonstrated in epitaxial "self-assembled" quantum dots (QDs) doped with single Mn²⁺ ions,[23−27] making these materials potentially attractive for quantum information processing[28] and solitary dopant optoelectronics ("solotronics").[29] Colloidal Mn²⁺-doped QDs with strong quantum confinement have shown spontaneous

photomagnetization[30] and charge-controlled magnetization[31] at elevated temperatures, both involving orientation of localized Mn²⁺ spins by delocalized charge carriers via strong *sp-d* exchange coupling. Energy gap tuning using the quantum confinement effect has revealed intrinsic dual emission in colloidal Mn²⁺-doped semiconductor nanocrystals,[7,32,33] and phase transfer into aqueous solution has opened doors for application of colloidal Mn²⁺-doped semiconductor nanocrystals in bioimaging.[33−36]

Recently, three groups have reported PL saturation with increasing excitation power in colloidal Mn²⁺-doped semiconductor nanocrystals.[37−39] One group has attributed Mn²⁺ PL saturation to complete depletion of ground-state Mn²⁺ in the nanocrystals.[37] Another has described saturation from Mn²⁺ photoionization via two sequential absorption/energy-transfer cycles, generating Mn³⁺ plus a hot electron.[38] The third describes saturation from exciton−exciton Auger recombination prior to energy transfer to Mn²⁺.[39] These experiments were all performed using very large pulse energies (up to 20 mJ/cm²) to achieve multiple photoexcitation events per nanocrystal within single laser pulses. Although the PL saturation in colloidal nanocrystals may at first appear similar to that in bulk, key experimental differences are evident: whereas PL saturation in bulk becomes more facile with increasing Mn²⁺ concentration, in the nanocrystals it becomes less facile,[37] and whereas PL saturation in bulk is characterized by a reduction in Mn²⁺ PL decay time, the nanocrystals show no change in Mn²⁺ PL decay times in the saturation regime.[38] The dominant process underlying PL saturation in Mn²⁺-doped semiconductor nanocrystals thus appears to be fundamentally different from

the one that dominates in bulk semiconductors. Given the broad interest in $Mn^{2+}$-doped semiconductor nanocrystals for optical imaging, magneto-optics, and photophysics, as well as the general historical importance of $Mn^{2+}$-doped semiconductor phosphors, a thorough understanding of these PL nonlinearities in $Mn^{2+}$-doped semiconductor nanocrystals is needed.

Here, we describe the excitation power dependence of PL from colloidal $Mn^{2+}$-doped II—VI nanocrystals under continuous-wave (CW) and quasi-CW photoexcitation conditions. A sublinear dependence of the time-integrated $Mn^{2+}$ PL on excitation power is observed even at very low excitation powers, with complete saturation achieved using only modest excitation powers. The nanocrystal PL quantum yields are reduced by over an order of magnitude traversing from the low-power limit to the saturation regime. Two-pulse photoexcitation measurements unambiguously demonstrate that the reduction in quantum yield is associated with the population of excited $Mn^{2+}$ ions. Time-resolved PL measurements implicate a fast (picosecond) nonradiative Mn*—exciton Auger-type cross relaxation as the fundamental origin of the PL saturation. These results are simulated using a kinetic model that accounts for Mn*—exciton cross relaxation explicitly, from which a cross-relaxation rate constant of at least $2 \times 10^{10}$ s$^{-1}$ is determined. These results emphasize the importance of the very long $Mn^{2+}$ $^4T_1$ excited-state lifetime in governing the photophysical properties of $Mn^{2+}$-doped semiconductor nanocrystals and have implications for future applications of such nanophosphors involving high-power photoexcitation.

## II. EXPERIMENTAL SECTION

**A. Synthesis and General Characterization.** $Mn^{2+}$-doped CdS, and core-doped core/shell ZnSe/ZnS and core/multishell ZnSe/ZnS/CdS/ZnS nanocrystals were synthesized as described previously.[33,40] $Mn^{2+}$:ZnSe nanocrystals were made by thermal decomposition of the tetramer $(Me_4N)_2[Zn_4(SePh)_{10}]$ in the presence of $MnCl_2$.[41] These nanocrystals were then coated with ZnS or CdS shells by successive slow additions of zinc- or cadmium oleate and trioctylphosphine sulfide.[42,43] $Mn^{2+}$:CdS nanocrystals were made by injecting a solution of S in octadecene into a hot (305 °C) solution of CdO and $Mn(OAc)_2$ in oleic acid, oleyl amine, and octadecene.[44] Samples were characterized by electronic absorption spectroscopy, transmission electron microscopy (TEM), inductively coupled plasma mass spectrometry (ICP-MS), electron paramagnetic resonance (EPR) spectroscopy, and PL quantum yield measurements (Hamamatsu integrating sphere). Relevant results from these characterization experiments are included in the Supporting Information. Unless otherwise stated, the results presented in this manuscript were collected using $Mn^{2+}$:ZnSe/ZnS/CdS/ZnS nanocrystals (= $Zn_{0.9955}Mn_{0.0045}$Se/ZnS/CdS/ZnS QDs), which showed the greatest photostability, but similar results were obtained for all systems studied. The results from parallel experiments performed on $Mn^{2+}$:ZnSe/ZnS nanocrystals are included in the Supporting Information.

**B. Photoluminescence Measurements.** PL samples were prepared by sandwiching drop-coated films of QDs between two sapphire disks. Films were prepared to have optical densities below 0.1 at the excitation wavelength. A brass foil with a 500 $\mu$m pinhole was mounted on the outside of the disks, and the samples were cooled to 7.5 K in a He flow cryostat. Illumination and PL collection were both performed

through the pinhole to ensure a uniform excitation density and to reduce the effects of scattering. The experimental results were influenced by the excitation beam intensity profile, with Gaussian profiles yielding noticeably less defined saturation curvature than the top-hat profiles provided by use of the pinhole. Laser powers were measured with a Coherent Lab-max power meter using an LM-2 UV head. Powers measured before the cryostat were converted to power density by measuring the fraction of the beam that passed through the pinhole in the absence of sample, accounting for losses due to reflection off the cryostat windows. A shutter was inserted in front of the cryostat to minimize possible long-term radiation damage.

The UV lines of an $Ar^+$ ion laser (~357 nm) were used for CW photoexcitation. Quasi-CW PL measurements were performed using the frequency doubled output of a Ti:Sapphire laser (150 fs pulses, 76 MHz, ~385 nm). The excitation beam was collimated to a diameter of 3 mm and brought into the sample at a steep angle (~10°).

Time-integrated PL spectra were collected by passing the collected light through a fiber to a monochromator (0.5 m, 150 g/mm grating blazed at 500 nm) equipped with an LN$_2$-cooled CCD detector. Each spectrum was collected over a 5 s integration window. All variable-power measurements were performed both by increasing and by decreasing the power across the full power range to ensure the absence of radiation damage. Time-resolved PL data were collected using a streak camera mounted on a 0.5 m monochromator (50 g/mm, 600 nm blaze). The single-pulse excitation experiments were performed using the 337 nm output of an N$_2$ laser operating at 18 Hz with a pulse duration of ~0.8 ns. Time-resolved PL was measured using a PMT and a multichannel scalar. The two-pulse variable delay experiments were performed using the Ti:Sapphire output and a pulse picker triggered by a function generator. This configuration allowed photons to be delivered to the sample in pairs of pulses every 10 ms, with variable delay between the two pulses, and with constant time-integrated power. For these experiments only, the beam was focused to a spot size of ~50 $\mu$m on the sample, resulting in energy densities reaching ~16 $\mu$J/cm$^2$.

## III. RESULTS

**A. Photoluminescence Power Dependence.** Figure 1 summarizes the excitation power dependence of the time integrated PL for a series of $Mn^{2+}$-doped II—VI semiconductor nanocrystals, measured at 7.5 K under CW and quasi-CW excitation conditions. Low temperatures were used in these measurements to eliminate potential contributions from laser heating on PL quantum yields and lifetimes (the PL quantum yield of the $Mn^{2+}$:ZnSe/ZnS/CdS/ZnS nanocrystals was temperature independent below ~200 K; see Supporting Information), but similar results were also obtained at room temperature.

Figure 1A shows PL spectra collected for $Mn^{2+}$:ZnSe/ZnS/CdS/ZnS nanocrystals at several CW excitation powers. The spectra are dominated by the intense $Mn^{2+}$ $^4T_1 \rightarrow {}^6A_1$ luminescence band centered at 590 nm, and also show weak excitonic luminescence centered at 445 nm. The $Mn^{2+}$ PL intensity increases with increasing excitation power over the experimental power range of 1–20 mW (<0.1–1.1 W/cm$^2$), but the increase is not linearly proportional to the excitation power. At high excitation powers, the $Mn^{2+}$ PL becomes independent of excitation power. In contrast, the excitonic PL intensity increases linearly with increasing excitation power
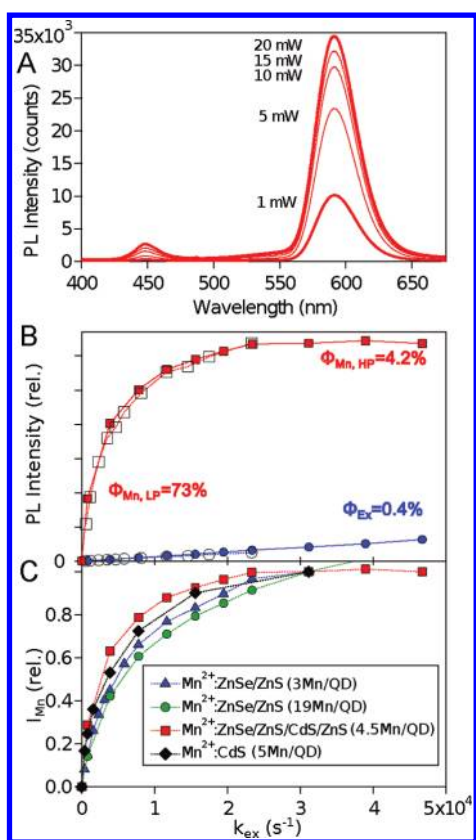
**Figure 1.** (A) Power dependence of the time-integrated, 7.5 K PL from $Mn^{2+}$:ZnSe/ZnS/CdS/ZnS QDs under CW excitation. 20 mW in this experiment corresponds to 1.1 $W/cm^2$ and $k_{ex} \approx 2.3 \times 10^4$ $s^{-1}$ (see text). (B) The integrated $Mn^{2+}$ (squares) and excitonic (circles) PL intensities of the same sample plotted versus $k_{ex}$ from both CW (open) and quasi-CW (filled) excitation. (C) Normalized $Mn^{2+}$ PL intensities from several $Mn^{2+}$-doped nanocrystals plotted versus $k_{ex}$. Squares: $Zn_{0.9955}Mn_{0.0045}$Se/ZnS/CdS/ZnS QDs (avg. 4.5 $Mn^{2+}$/QD, $d$ = 6.0 nm, $E_g$ = 2.8 eV). Circles: $Zn_{0.984}Mn_{0.016}$Se/ZnS QDs (avg. 19 $Mn^{2+}$/QD, $d$ = 6.0 nm, $E_g$ = 3.0 eV). Triangles: $Zn_{0.995}Mn_{0.005}$Se/ZnS QDs (avg. 3 $Mn^{2+}$/QD, $d$ = 3.5 nm, $E_g$ = 3.1 eV). Diamonds: $Cd_{0.995}Mn_{0.005}$S QDs (avg. 5 $Mn^{2+}$/QD, $d$ = 4.5 nm, $E_g$ = 2.8 eV). For comparison, the data are normalized at $k_{ex}$ = 3.1 × 10⁴ $s^{-1}$.

over the entire power range. In addition to these two PL features, a weak, broad PL band is evident near the $Mn^{2+}$ PL peak. This broad band is attributed to surface-trap emission. This PL is readily separated from that of the $Mn^{2+}$ because of its linear power dependence.

Figure 1B plots the integrated $Mn^{2+}$ and excitonic PL intensities from Figure 1A vs nanocrystal excitation rate constant, along with similar data collected using quasi-CW excitation. The excitation rate constant is defined as $k_{ex} = \sigma q_p$, where $\sigma$ is the nanocrystal absorption cross section at the excitation wavelength, and $q_p$ is the photon flux. For example, for the quasi-CW data in Figure 1B, careful measurement through a pinhole centered in the cryostat gave an irradiation intensity of $I_{max}$ = 5 $W/cm^2$ at the maximum laser power of 60 mW ($\lambda$ = 385 nm), corresponding to a photon flux $q_p = I/h\nu = 10^{19}$ $s^{-1}cm^{-2}$. A value of $\sigma \sim 5 \times 10^{-15}$ $cm^2$ was estimated at this wavelength from literature oscillator strengths.[45,46] Together, these values give an excitation rate constant of $k_{ex} \approx 5 \times 10^4$ $s^{-1}$ at $I_{max}$ for this particular measurement.

The CW and quasi-CW excitation modes yielded indistinguishable PL results. For both, sublinear $Mn^{2+}$ PL power

dependence was observed at all excitation rate constants, even below $\sim 5 \times 10^3$ $s^{-1}$. At an excitation rate constant of $5 \times 10^4$ $s^{-1}$, the $Mn^{2+}$ PL was completely saturated. Because of this strongly sublinear power dependence, the $Mn^{2+}$ PL quantum yield also changed with excitation power. In the low power limit, the quantum yield was 73%. At the highest power in Figure 1B, the quantum yield had dropped to only 4.2%. $Mn^{2+}$ PL in doped semiconductor nanocrystals is thus highly nonlinear even with modest CW excitation powers. In contrast to the $Mn^{2+}$ PL saturation, the excitonic intensity increased linearly with excitation power over the entire power range examined here, having a constant quantum yield of ∼0.4%.

$Mn^{2+}$-doped nanocrystals of several different compositions were examined, and all showed similar $Mn^{2+}$ PL saturation. Figure 1C plots the data from four different samples including those of Figure 1A,B as well as $Mn^{2+}$:CdS and $Mn^{2+}$:ZnSe/ZnS nanocrystals. Despite differences in PL decay times (both $Mn^{2+}$ and excitonic), $Mn^{2+}$ concentrations, and PL quantum yields, saturation was observed over a similar range of $k_{ex}$ in all samples. These results indicate that facile $Mn^{2+}$ PL saturation is a general property of $Mn^{2+}$-doped semiconductor nanocrystals.

**B. Time-Resolved Photoluminescence.** Figure 2 plots the $Mn^{2+}$ $^4T_1 \rightarrow {}^6A_1$ PL decay versus time, measured following
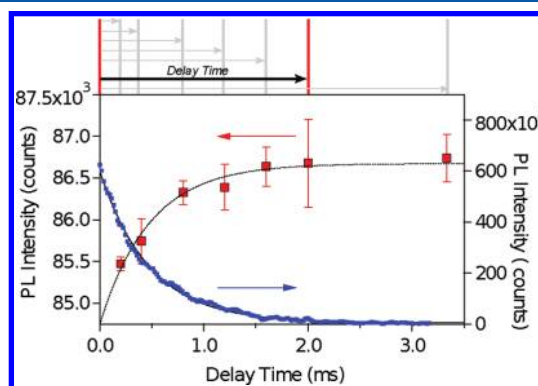


**Figure 2.** Right axis: $Mn^{2+}$ PL decay in the $Mn^{2+}$:ZnSe/ZnS/CdS/ZnS nanocrystals of Figure 1. The solid line shows a single exponential decay curve with $\tau$ = 379 $\mu s$. Left axis: Integrated $Mn^{2+}$ PL intensity measured with pairs of excitation pulses, plotted as a function of the delay time between the two pulses. The top panel depicts this experiment schematically. Error bars represent standard deviations of four measurements. The gray dashed line shows the $\tau$ = 379 $\mu s$ decay of the $Mn^{2+}$ PL. Data measured at 7.5 K.

pulsed excitation. This PL decay is characterized by a single exponential with $\tau_{Mn}$ = 379 $\mu s$, consistent with previous measurements on related samples.[8] On the same time axis, Figure 2 also plots integrated $Mn^{2+}$ PL intensities measured using pairs of excitation pulses with long delay times between pairs. The data are plotted as a function of the delay time between the two pulses in each pair (top, see Experimental Section). These experiments were performed with 16 $\mu J/cm^2$ excitation power at 385 nm, with which ∼10% of the nanocrystals were excited per pulse. Starting from delay times well beyond the $Mn^{2+}$ $^4T_1$ lifetime (>3 ms), the points in Figure 2 show that the integrated $Mn^{2+}$ PL intensity decreased as the two pulses were brought closer together. The change in integrated $Mn^{2+}$ PL intensity plotted versus delay time between pulses is characterized by a single exponential with the same apparent time constant as the $Mn^{2+}$ $^4T_1$ PL decay (∼379 $\mu s$). This result identifies the reduction in $Mn^{2+}$ PL intensity in

Figure 2 as arising from photoexcitation of nanocrystals by the second pulse within the $Mn^{2+}$ $^4T_1$ excited-state lifetime of the first excitation pulse, i.e., photoexcitation of nanocrystals that already contain excited $Mn^{2+}$. By extension, these results allow the conclusion that the PL saturation in Figure 1 also arises from photoexcitation of nanocrystals that already contain excited $Mn^{2+}$. By correlating it with the $Mn^{2+}$ excited-state population, other possible origins of the PL saturation such as laser heating[47] or photocharging[48] are excluded.

Figure 3 summarizes the influence of excitation power on the $Mn^{2+}$:ZnSe/ZnS/CdS/ZnS nanocrystal PL time dependence
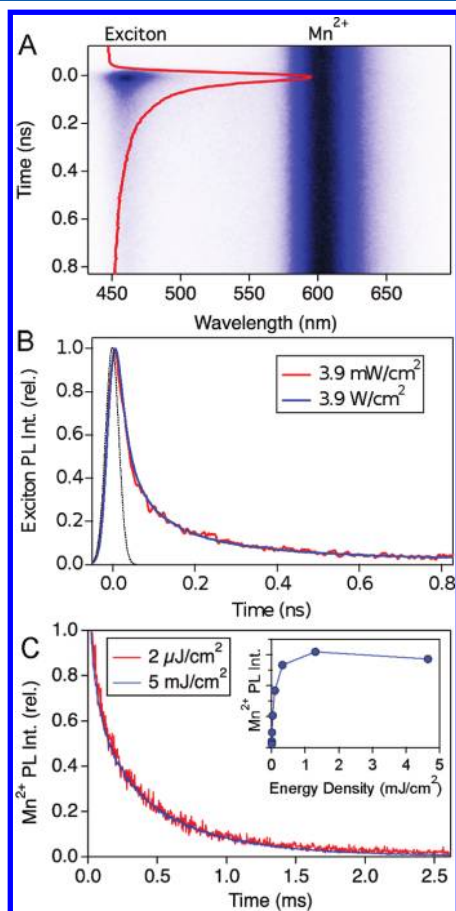


**Figure 3.** (A) Streak camera image (7.5 K, 0.4 W/cm$^2$) showing the time dependence of the excitonic and $Mn^{2+}$ PL from the $Mn^{2+}$:ZnSe/ZnS/CdS/ZnS nanocrystals of Figure 1. The red line plots the excitonic luminescence intensity (integrated between 439 and 481 nm) versus time. (B) Excitonic PL measured using low- and high-power excitation, both at 7.5 K. The dotted line represents the instrument response function. (C) $Mn^{2+}$ PL decay traces collected with low- and high-power pulsed excitation at 7.5 K (18 Hz repetition rate, 337 nm). The inset shows saturation of the integrated $Mn^{2+}$ PL with increasing pulse energy density under the same experimental conditions.

using quasi-CW excitation conditions (150 fs pulses, 76 MHz repetition rate). Figure 3A shows a streak camera image collected following an excitation pulse at time = 0. The $Mn^{2+}$ PL intensity is effectively constant over the entire dark time between excitation pulses (13 ns). On the other hand, the excitonic PL shows a burst of intensity, followed by decay.

Figure 3B plots normalized excitonic PL decay traces collected at low and high excitation powers. These excitonic

PL decay traces are fit well using a biexponential function with two distinct time constants, $\tau_1$ = 29 ps and $\tau_2$ = 308 ps. The fast and slow components account for 34% and 66% of the overall excitonic PL. Exciton-to-$Mn^{2+}$ energy transfer takes place within a few tens of picoseconds.[4−7] The excitonic PL having $\tau_2$ = 308 ps thus decays too slowly to come from doped QDs, and is attributed to undoped QDs. The excitonic PL decay time of $\tau_1$ = 29 ps agrees well with those of other doped QDs, and this component is thus assigned to doped QDs. $\tau_1$ = 29 ps is close to the instrument response function, and faster decay would not be resolved. This value is therefore considered a measure of the slowest energy transfer processes within the ensemble of doped QDs. These assignments are supported by analysis of $Mn^{2+}$ distributions within the ensemble of nanocrystals (*vide infra*).

Figure 3B also demonstrates that the excitonic PL decay dynamics are unchanged over the excitation power range in which the $Mn^{2+}$ PL saturates and its quantum yield decreases by an order of magnitude. As discussed in the Analysis section, this result implies that the nonradiative processes responsible for $Mn^{2+}$ saturation occur on the same time scale as exciton-to-$Mn^{2+}$ energy transfer.

Figure 3C plots the $Mn^{2+}$ PL decay measured following pulsed excitation at low and high excitation powers (18 Hz repetition rate, 337 nm). The inset illustrates PL saturation at the high-power conditions used for this measurement. There is no discernible change in $Mn^{2+}$ PL decay time upon traversing from low- to high-power excitation, indicating that PL saturation is not associated with a reduction in the intrinsic $Mn^{2+}$ PL quantum yield.

## IV. ANALYSIS

**A. Staircase Excitation Model.** Figure 4A describes the well-established scheme by which a nanocrystal containing $m$ $Mn^{2+}$ dopants is photoexcited. After photoexcitation of the nanocrystal (with rate constant $k_{ex}$), the resulting exciton (QD*) can recombine ($k_{QD}$) or be quenched via nonradiative energy transfer to $Mn^{2+}$ ($m \cdot k_{et}$). The excited $Mn^{2+}$ (Mn*) decays with rate constant $k_{Mn}$. The rate constants $k_{QD}$ and $k_{Mn}$ described here represent the sum of radiative and nonradiative contributions. All four of the above rate constants ($k_{ex}$, $k_{QD}$, $k_{et}$, $k_{Mn}$) have been determined experimentally.

Figure 4B illustrates how the excited state dynamics may change when the excitation rate is large enough that the nanocrystal absorbs a second photon while one of the $Mn^{2+}$ dopants is still in its excited state from a preceding photoexcitation event. This situation introduces new Auger-type cross-relaxation processes. Two types of cross relaxation can be distinguished on the basis of their final states (exciton or $Mn^{2+}$($^4T_1$)), and these are indicated by the rate constants $k_{a1}$ and $k_{a2}$, respectively. For example, the excited $Mn^{2+}$ may transfer its energy to the exciton to yield ground-state $Mn^{2+}$ and a hot exciton, which may then relax nonradiatively to return to QD*. Similarly, the exciton may transfer its energy to Mn* to yield an upper $Mn^{2+}$ excited state, which may then relax nonradiatively back to the $^4T_1$ state. The possibility of branching between the exciton and $Mn^{2+}$($^4T_1$) final states during relaxation is also accounted for in this model. In all processes, thermalization is assumed to be rapid relative to luminescence.

Figure 4C extends the scenario of Figure 4B to account for any arbitrary number of sequential excitations per nanocrystal, including the possibility of exciting all $Mn^{2+}$ ions to their $^4T_1$
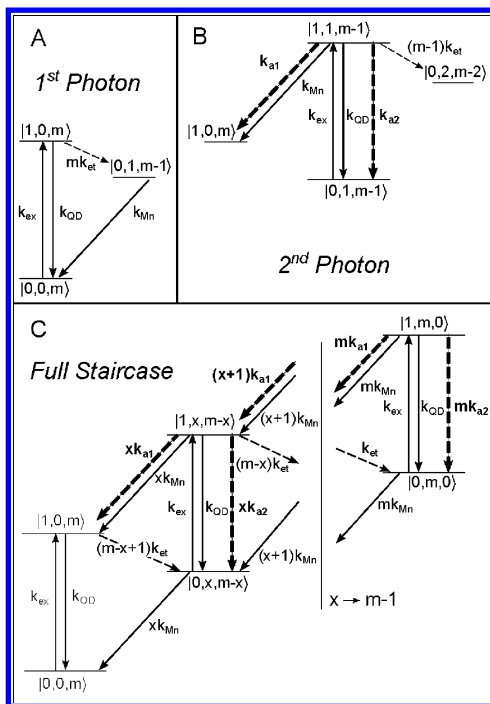
**Figure 4.** (A) Schematic description of low-power photoexcitation of a Mn$^{2+}$-doped nanocrystal containing $m$ Mn$^{2+}$ ions. QD $\rightarrow$ QD* photoexcitation proceeds with a rate constant of $k_{ex}$. The photoexcited QD can relax by recombination ($k_{QD}$) or by energy transfer to Mn$^{2+}$ ($k_{et}$). The excited-state Mn$^{2+}$ relaxes with $k_{Mn}$. States are denoted by the number of excitons, the number of excited-state Mn$^{2+}$ ions, and the number of ground-state Mn$^{2+}$ ions, i.e., |#QD*, #Mn*, #Mn⟩. (B) Schematic description of photoexcitation of a Mn$^{2+}$-doped QD that already contains an excited-state Mn$^{2+}$ ion. In addition to recombination and energy transfer to Mn$^{2+}$, QD* may now relax via one of two Auger cross-relaxation processes ($k_{a1}$ and $k_{a2}$), differentiated by their final states. (C) In a nanocrystal with $m$ Mn$^{2+}$ ions, multiple sequential photoexcitation events can yield $x \leq m$ excited Mn$^{2+}$ ions, with corresponding changes in cross-relaxation and energy-transfer rates.

excited states. This "staircase" excitation scheme forms the basis of the kinetic model employed here. For small $k_{ex}$ relative to $k_{et}$ and $k_{QD}$, eqs 1 and 2 describe the population dynamics implied by Figure 4C in terms of a set of coupled differential equations for a nanocrystal containing $m$ Mn$^{2+}$ dopants, for $x = 0, 1, 2, ...,$ $m$, where $x$ is the number of excited Mn$^{2+}$ ions in that nanocrystal. Equation 1a describes the Mn* population dynamics. In the special case of $x = 0$, eq 1b applies.

$$\frac{d|QD, x\text{Mn}^*, (m-x)\text{Mn}\rangle}{dt}$$
$$= -(k_{ex} + xk_{Mn})|QD, x\text{Mn}^*, (m-x)\text{Mn}\rangle$$
$$+ (m-x+1)k_{et}|QD^*, (x-1)\text{Mn}^*,$$
$$(m-x+1)\text{Mn}\rangle + (k_{QD} + xk_{a2})|QD^*, x\text{Mn}^*,$$
$$(m-x)\text{Mn}\rangle + (x+1)k_{Mn}|QD,$$
$$(x+1)\text{Mn}^*, (m-x-1)\text{Mn}\rangle \quad (1a)$$

$$\frac{d|QD, 0\text{Mn}^*, m\text{Mn}\rangle}{dt}$$
$$= -k_{ex}|QD, 0\text{Mn}^*, m\text{Mn}\rangle + k_{QD}|QD^*, 0\text{Mn}^*, m\text{Mn}\rangle$$
$$+ k_{Mn}|QD, 1\text{Mn}^*, (m-1)\text{Mn}\rangle \quad (1b)$$

Similarly, eq 2 describes the excitonic (QD*) population dynamics implied by Figure 4C.

$$\frac{d|QD^*, x\text{Mn}^*, (m-x)\text{Mn}\rangle}{dt}$$
$$= -(k_{QD} + xk_{Mn} + xk_{a1} + xk_{a2}$$
$$+ (m-x)k_{et})|QD^*, x\text{Mn}^*, (m-x)\text{Mn}\rangle$$
$$+ k_{ex}|QD, x\text{Mn}^*, (m-x)\text{Mn}\rangle$$
$$+ (x+1)(k_{Mn} + k_{a1})|QD^*, (x+1)\text{Mn}^*,$$
$$(m-x-1)\text{Mn}\rangle \quad (2a)$$

For the special case of $x = m$, eq 2b applies:

$$\frac{d|QD^*, m\text{Mn}^*, 0\text{Mn}\rangle}{dt}$$
$$= -(k_{QD} + mk_{Mn} + mk_{a1} + mk_{a2})|QD^*,$$
$$m\text{Mn}^*, 0\text{Mn}\rangle + k_{ex}|QD, m\text{Mn}^*, 0\text{Mn}\rangle \quad (2b)$$

In formulating eqs 1 and 2, three assumptions have been made: (i) $k_{ex}$ does not depend on the number of excited Mn$^{2+}$ ions in the QD; (ii) the effective energy-transfer rate constant from the exciton to Mn$^{2+}$ is proportional to the number of Mn$^{2+}$ in the ground state and can be written as $k_{eff} = (m-x)k_{et}$, where $k_{et}$ is the rate constant for transfer in a nanocrystal with a single Mn$^{2+}$; (iii) because the upper excited states formed via both cross-relaxation processes relax very quickly to their respective lowest excited states by internal conversion, the rate constants $k_{a1}$ and $k_{a2}$ are rate limiting. Like $k_{et}$, $k_{a1}$ and $k_{a2}$ are assumed to be additive per excited Mn$^{2+}$. Finally, in using effective rate constants, distributions in energy transfer and cross-relaxation rate constants due to nanocrystal size or dopant-position distributions are neglected.

By solving eqs 1 and 2 for continuous irradiation, the steady state populations at each level in the staircase scheme of Figure 4B can be calculated. Importantly, all of the necessary rate constants are known from independent experiments, except for $k_{a1}$ and $k_{a2}$. $k_{ex}$ is determined from the measured power density and the literature absorption cross section of ZnSe ($5 \times 10^{-15}$ cm$^2$).[45] The other rate constants were determined here: $k_{Mn} = 2640$ s$^{-1}$ from Figure 2, and $k_{QD} = 3 \times 10^9$ s$^{-1}$ from the slow component of Figure 3B. From the fast component of Figure 3B, we estimate $k_{et} \geq \sim 3 \times 10^{10}$ s$^{-1}$, and a value of $k_{et} = 5 \times 10^{10}$ s$^{-1}$ is taken for the model calculations. This effective rate constant encompasses variations due to distributions in QD size or Mn$^{2+}$ position. To convert excited state populations to PL intensities, the populations calculated from eqs 1 and 2 were scaled by the quantum yields and lifetimes of the two emissive excited states, which were either measured directly or determined from experimental data using the calculated dopant distribution (see below). In all model calculations reported here, the Auger cross-relaxation rate constants are therefore the only variable parameters. From the data in Figure 3B, the cross-relaxation rate constant is estimated to be on the same order of magnitude as $k_{et}$ for the following reasons: In the limit of slow

cross relaxation, the apparent exciton decay time would increase upon $Mn^{2+}$ PL saturation, but no increase is observed. Similarly, in the limit of fast cross relaxation, the apparent exciton decay time would decrease upon $Mn^{2+}$ PL saturation, but this decrease is not observed. An initial trial value of $5 \times 10^{10}$ s$^{-1}$ ($\approx k_{et}$) was therefore taken for the model calculations. As described in Section IV.C (below), simulations of the power dependence data using eqs 1 and 2 ultimately yield a cross-relaxation rate constant of $>2 \times 10^{10}$ s$^{-1}$.

$Mn^*$–$Mn^*$ annihilation was purposely omitted from this model. The data in Figure 3C and those reported previously in ref 38 for related CdS/$Mn^{2+}$:ZnS nanocrystals demonstrate that the $Mn^{2+}$ PL decay time is unaltered in the saturation regime. This behavior contrasts with the reduced $Mn^{2+}$ PL lifetimes observed with increased excitation densities in related bulk materials, which suggested $Mn^*$ energy migration followed by $Mn^*$–$Mn^*$ cross relaxation.[11−15] Such processes occur on the 10 $\mu$s time scale,[14,15] and they become slower at lower $Mn^{2+}$ concentrations.[49] $Mn^*$–$Mn^*$ cross relaxation is therefore far too slow to be responsible for the PL saturation in Figures 1−3.

Exciton–exciton Auger relaxation has also been deliberately omitted. Under the CW or quasi-CW excitation conditions used here, the excitation rate constants are too small to photoexcite a QD twice within the exciton lifetimes found in Figure 3. Exciton–exciton Auger relaxation can therefore be ruled out as the origin of the $Mn^{2+}$ PL saturation in Figures 1−3.

**B. Dopant Distributions.** A realistic description of the distribution of $Mn^{2+}$ within the experimental ensemble of nanocrystals is critical. Whereas analytical techniques provide the global average number of $Mn^{2+}$ per average QD ($\bar{m}$), it is generally recognized that these $Mn^{2+}$ are distributed among the QDs according to Poissonian statistics. Figure 5 plots the
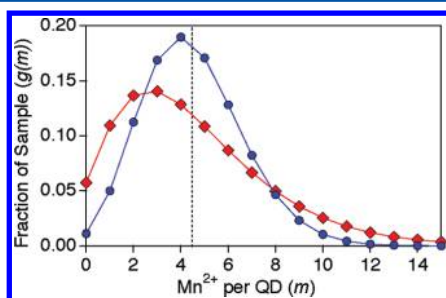


**Figure 5.** Distributions of $Mn^{2+}$ ions over the ensemble of $Mn^{2+}$:ZnSe/ZnS/CdS/ZnS nanocrystals from the sample of Figure 1, possessing $Mn^{2+}$:ZnSe cores with an average diameter of $d_{avg} = 4.5$ nm and an average number of $Mn^{2+}$/QD of $\bar{m} = 4.5$. The dashed line indicates the average of $\bar{m} = 4.5$ $Mn^{2+}$/QD. The circles indicate the Poissonian distribution calculated for uniform $d = 4.5$ nm nanocrystals. The diamonds indicate the distribution calculated by folding the Poissonian dopant distribution with a Gaussian nanocrystal size distribution for $d_{avg} = 4.5$ nm, $\sigma = 0.85$ nm. See Appendix for details.

Poissonian distribution expected for $\bar{m} = 4.5$. In any real sample, however, the QD size distribution is also an important aspect of the dopant distribution, because small changes in diameter correspond to large changes in nanocrystal volume. Figure 5 therefore also plots the distribution of $Mn^{2+}$ ions ($\bar{m} = 4.5$) within an ensemble of $d_{avg} = 4.5$ nm nanocrystals (core diameter of the QDs used for Figures 1-3) with a Gaussian distribution in particle diameter described by a half-width of 2 nm (or $\sigma = 0.85$ nm, as estimated from the absorption

spectrum), obtained by calculating a Poissonian distribution of dopants at each QD volume within the size distribution (see Appendix). This more realistic distribution is broader than the one obtained for uniform $d = 4.5$ nm nanocrystals. Specifically, more nanocrystals contain no $Mn^{2+}$, and more nanocrystals contain larger numbers of $Mn^{2+}$. For the kinetics calculations, differential equations were generated and solved for each value of $m$ within this distribution.

**C. Results of the Model Calculations.** Figure 6A shows the steady-state $Mn^{2+}$ excited-state populations calculated from
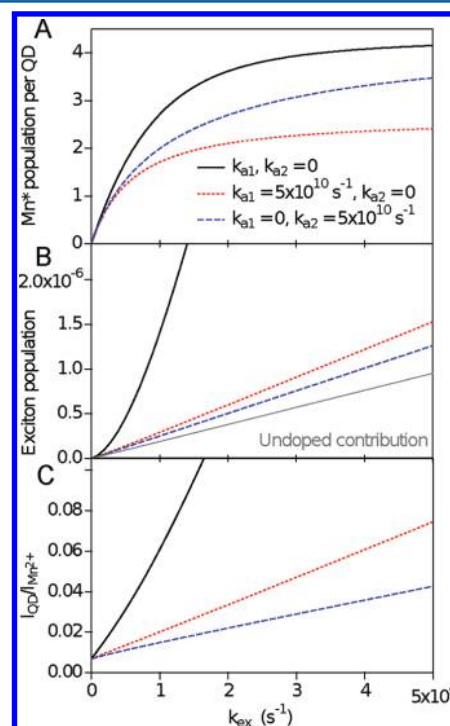


**Figure 6.** (A) $Mn^{2+}$ excited-state population per QD as a function of the excitation rate constant $k_{ex}$ for no Auger cross relaxation (—), for cross relaxation via $k_{a1} = 5 \times 10^{10}$ s$^{-1}$ ($\cdots$), and for cross relaxation via $k_{a2} = 5 \times 10^{10}$ s$^{-1}$ (---). (B) Exciton population as a function of $k_{ex}$ for the same values of $k_{a1}$ and $k_{a2}$. The contribution from undoped QDs is shown in gray. (C) The ratio of exciton to $Mn^{2+}$ steady-state PL intensities as a function of $k_{ex}$ for the same values of $k_{a1}$ and $k_{a2}$.
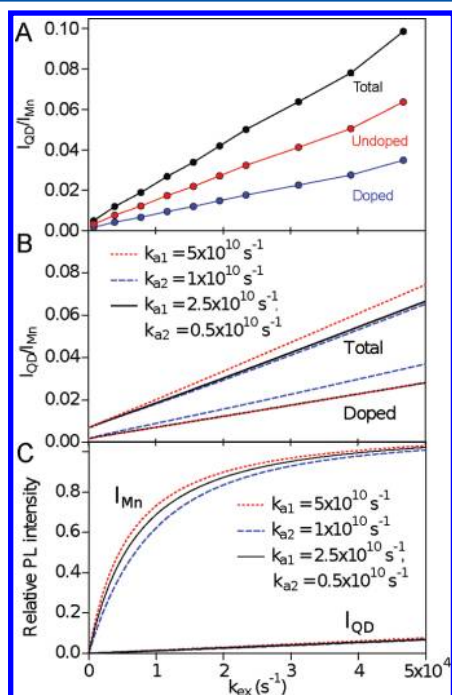
eqs 1 and 2 as a function of $k_{ex}$ without any Auger quenching ($k_{a1} = k_{a2} = 0$), and with $k_{a1}$ and $k_{a2}$ independently set to $5 \times 10^{10}$ s$^{-1}$, the value estimated from Figure 3B. All three curves show population saturation in the same range of $k_{ex}$. Without any cross relaxation, the population distribution asymptotically approaches the limit in which all 4.5 $Mn^{2+}$/QD are in their $^4T_1$ excited state. This approach is slow because of the broad tailing distribution in $Mn^{2+}$/QD at large values (Figure 5). When cross relaxation occurs with $Mn^{2+}$ $^4T_1$ as its final state ($k_{a2}$), this same asymptote is approached, but more slowly. When the excitonic state is the final state of the cross-relaxation process ($k_{a1}$), saturation is reached with only about half of the total $Mn^{2+}$/QD in their excited state.

The exciton population is even more sensitive to the Auger processes, as shown in Figure 6B. Without any cross relaxation, the exciton population rises rapidly and superlinearly as all of the $Mn^{2+}$ become excited (solid curve). With Auger quenching, however, its dependence on $k_{ex}$ becomes linear and is dominated by the undoped subset. The effects of $k_{a1}$ and $k_{a2}$

are very similar in this regard, but $k_{a2}$ is slightly more effective at quenching the excitonic population.

Experimentally, it is easier to obtain accurate *relative* exciton and $Mn^{2+}$ luminescence intensities than it is to obtain accurate absolute luminescence quantum yields of either independently. It is therefore valuable to explore how the ratio of these two intensities ($I_{QD}/I_{Mn}$) may reflect the proposed quenching processes. Figure 6C replots the calculated results from Figure 6B in this fashion and reveals important differences in $I_{QD}/I_{Mn}$ for different Auger cross-relaxation rate constants. In the absence of cross relaxation, $I_{QD}/I_{Mn}$ increases superlinearly to very large values over the experimental range of $k_{ex}$, reaching 0.38 at the right side of the plot. $I_{QD}/I_{Mn}$ decreases substantially when Auger cross relaxation is introduced (either $k_{a1}$ or $k_{a2} \neq 0$), and its dependence on $k_{ex}$ becomes more linear. In addition, the value of the ratio at the maximum $k_{ex}$ decreases with increasing cross relaxation rate constants. These changes reflect in part the greater relative contribution of the undoped QDs to the excitonic PL when cross relaxation is active. For illustration, setting $k_{a1} = k_{et}$ or $k_{a2} = k_{et}$ gives the two curves shown in Figure 6C. These curves have values of $I_{QD}/I_{Mn}$ = 0.074 and 0.043, respectively, at $k_{ex} = 5 \times 10^4$. Figure 6C thus illustrates that plotting $I_{QD}/I_{Mn}$ versus $k_{ex}$ allows assessment of the cross-relaxation rate constant. Additionally, the intercept at $k_{ex} = 0$ in Figure 6C is independent of cross relaxation, being sensitive only to $k_{et}$ and the relative contributions of doped and undoped nanocrystals to $I_{QD}$. The excitonic PL from undoped QDs can therefore be used as an internal reference in this analysis.

Figure 7 therefore replots the $Mn^{2+}$ and excitonic PL intensities from Figure 1B as $I_{QD}/I_{Mn}$ versus $k_{ex}$ for comparison with the model calculations. In addition to $I_{QD}/I_{Mn}$, the contributions from doped and undoped QDs to $I_{QD}/I_{Mn}$ are plotted individually, as decomposed by the time-resolved PL data in Figure 3. $I_{QD}/I_{Mn}$ has an intercept of 0.0036 (0.0013 from doped QDs), and reaches a value of 0.10 (0.035 from doped QDs) at the right edge of the plot. Between these two values, the experimental power dependence of $I_{QD}/I_{Mn}$ is essentially linear.

As shown in Figure 7B, the experimental results are reproduced well using either $k_{a1} = 5 \times 10^{10}$ s$^{-1}$, $k_{a2} = 1 \times 10^{10}$ s$^{-1}$, or both parameters at half of these values. The calculated curves reproduce the linearity, slopes, intercepts, and relative contributions of doped and undoped (= total − doped; not plotted) QDs seen in the experimental data. Decreasing the cross-relaxation rate constant by less than 1 order of magnitude yields substantially different slopes and intercepts that do not reproduce the experimental results (*vide infra*). We therefore conclude that the cross-relaxation rate constant is ~$10^{10}$ s$^{-1}$ or faster.

With the kinetic parameters from Figure 7B, the individual PL intensities $I_{Mn}$ and $I_{QD}$ can now be calculated under the same conditions, and these results are presented in Figure 7C for comparison with Figure 1. The calculations show 2.4, 4.0, or 2.9 excited $Mn^{2+}$ per QD at $k_{ex} = 5 \times 10^4$ s$^{-1}$ for $k_{a1} = 5 \times 10^{10}$ s$^{-1}$, $k_{a2} = 1 \times 10^{10}$ s$^{-1}$, or both parameters at half of these values, respectively. For the same rate constants, excitonic steady-state populations reach only ~$10^{-6}$/per QD, with approximately two-thirds of this population originating from undoped particles.

The ability of the model calculations to determine the cross-relaxation rate constants quantitatively can be assessed by plotting $I_{QD}/I_{Mn}$ versus these rate constants. Figure 8A plots the
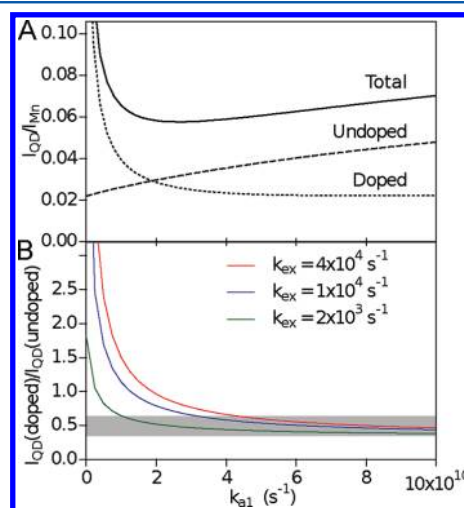


**Figure 7.** (A) Experimental PL ratios $I_{QD}/I_{Mn}$ plotted as a function of excitation rate constant, from the PL intensities presented in Figure 1B. The contributions from doped and undoped QDs to $I_{QD}$ are also plotted independently. (B) $I_{QD}/I_{Mn}$ calculated from eqs 1 and 2 using $k_{a1} \neq 0$, $k_{a2} \neq 0$, or a combination of the two. (C) $I_{QD}$ and $I_{Mn}$ calculated under the same conditions. At $k_{ex} = 5 \times 10^4$ s$^{-1}$, $Mn^{2+}$ excited-state populations were 2.4, 4.0, and 2.9 Mn*/QD for $k_{a1}$, $k_{a2}$, and the combination described in the legend.



**Figure 8.** (A) $I_{QD}/I_{Mn}$ calculated as a function of the cross-relaxation rate constant $k_{a1}$ at fixed $k_{ex} = 4 \times 10^4$ s$^{-1}$. The contributions from doped (···) and undoped (---) excitonic PL are plotted individually. (B) The ratio of doped to undoped excitonic PL as a function of cross-relaxation rate constant ($k_{a1}$), at several excitation rate constants. The shaded region indicates the ratio observed experimentally.

dependence of $I_{QD}/I_{Mn}$ on $k_{a1}$ for fixed $k_{ex} = 4 \times 10^4$ s$^{-1}$ (high power regime). Initially, $I_{QD}/I_{Mn}$ decreases sharply with increasing $k_{a1}$. At larger $k_{a1}$, however, $I_{QD}/I_{Mn}$ increases again gradually. Examination of the doped and undoped QD contributions individually shows that $I_{QD}$ at high powers is mostly due to undoped nanocrystals. For the doped subset,

$I_{QD}/I_{Mn}$ is large at small $k_{a1}$ but decreases sharply with increasing $k_{a1}$, asymptotically approaching a value of 0.02. The most significant aspect of Figure 8A is the crossing point around $k_{a1} = 2 \times 10^{10}$ s$^{-1}$, where the excitonic PL from undoped nanocrystals surpasses that from doped nanocrystals. From the experimental data in Figure 3, the excitonic PL from undoped QDs is twice that of doped QDs, indicating that the cross-relaxation rate constant in the experimental samples must be to the right of this crossing point. Reasonable agreement with experiment in both absolute values and relative contributions from doped and undoped QDs is achieved for $k_{a1} \sim 5 \times 10^{10}$ s$^{-1}$. A similar conclusion is obtained from analysis of the dependence of $I_{QD}/I_{Mn}$ on $k_{a2}$ (see Supporting Information).

Figure 8B plots the ratio of doped to undoped excitonic PL ($I_{QD}$(doped)/$I_{QD}$(undoped)) versus $k_{a1}$ for three excitation rates. For all three curves, the ratio decreases sharply with increasing $k_{a1}$ and then levels out. At small $k_{a1}$, the ratio depends strongly on $k_{ex}$, but at larger $k_{a1}$ the curves converge to a value close to the ratio measured experimentally ($\sim$0.5, Figures 3B and 7A), indicated by the shaded region. To reproduce $I_{QD}$(doped)/$I_{QD}$(undoped) quantitatively, including its independence from $k_{ex}$ (Figure 3B), the cross relaxation must have a rate constant of at least $4 \times 10^{10}$ s$^{-1}$. A similar analysis assuming only $k_{a2} \neq 0$ yields a lower limit of $k_{a2} = 2 \times 10^{10}$ s$^{-1}$ (see Supporting Information).

## V. DISCUSSION

Mn$^{2+}$ PL saturation has been observed at low CW and quasi-CW excitation powers for a variety of nanocrystals including Mn$^{2+}$-doped ZnSe, CdS, and core/multishell nanocrystals. Previous studies of Mn$^{2+}$ PL power dependence in Mn$^{2+}$-doped semiconductor nanocrystals used high-power pulsed excitation to achieve saturation, and saturation was attributed to multiexciton Auger recombination prior to energy transfer to Mn$^{2+}$,[39] excitation of all Mn$^{2+}$,[37] or sequential energy transfer to Mn$^{2+}$ causing Mn$^{2+/3+}$ ionization.[38] Because saturation occurs at low CW excitation rates (Figure 1), multiexciton Auger recombination can be ruled out. If Mn$^{2+}$ PL saturation resulted from sequential excitation of all Mn$^{2+}$ ions, excitonic PL intensities would increase superlinearly as Mn$^{2+}$ PL saturates, and exciton PL decay times would approach those of the undoped QDs. The results in Figures 1B and 3B demonstrate that this is not the case. PL saturation due to excitation of all Mn$^{2+}$ ions is therefore also ruled out. Nevertheless, two-pulse measurements (Figure 2) unambiguously link Mn$^{2+}$ PL saturation with photoexcitation of QDs that already contain Mn$^{2+}$ in its $^{4}T_1$ excited state.

From the rapid reduction in PL quantum yield, it is evident that Mn$^{2+}$ PL saturation is accompanied by efficient non-radiative deactivation. The experimental results implicate exciton−Mn$^{2+}$ cross relaxation as the primary process reducing Mn$^{2+}$ PL quantum yield with increasing excitation power. The analysis above demonstrates that this cross relaxation process has an effective rate constant comparable to that of energy transfer ($k_{et} = 5 \times 10^{10}$ s$^{-1}$). With inclusion of cross relaxation, the staircase excitation model (Figure 4, eqs 1 and 2) reproduces the experimental observations using a cross-relaxation rate constant of at least $2 \times 10^{10}$ s$^{-1}$, with all other input parameters fixed from experiment, capturing the essence of the PL saturation effect. We note that the curves shown in Figure 7 were generated without iterative fitting, which would undoubtedly yield better quantitative reproduction of the experimental data but would not improve our qualitative understanding of the underlying physical processes.

The kinetic model reproduces the main experimental observations, but it cannot definitively differentiate between the two possible microscopic processes of QD* → Mn* or Mn* → QD* energy transfer (described by $k_{a1}$ and $k_{a2}$, respectively). The microscopic mechanism behind the cross relaxation thus remains an open question. A previous report has suggested that cross relaxation involves donor-type ionization of Mn$^{2+}$ to form Mn$^{3+}$ and a "hot electron,"[38] which would be accounted for by $k_{a2}$ in eqs 1 and 2 assuming return to the Mn$^{2+}$ $^{4}T_1$ excited state upon cooling. For cross relaxation to cause Mn$^{2+/3+}$ ionization, however, the exciton must be sufficiently energetic to excite the Mn* into a photoionization state. The commonly referenced positions of the Mn$^{2+/3+}$ ionization levels in II−VI semiconductors, derived from resonant photoelectron spectroscopy (RPES), place the Mn$^{2+/3+}$ level $\sim$3.5 eV below the valence band edge for bulk Mn$^{2+}$:CdS, Mn$^{2+}$:ZnSe, and Mn$^{2+}$:ZnS.[50,51] As such, Mn$^{2+/3+}$ ionization to the conduction band from the $^{4}T_1$ state should *always* occur outside the semiconductor energy gap, and could therefore not be achieved with one additional quantum of band gap energy delivered via energy transfer. The similarity of the PL saturation across a variety of doped semiconductor nanocrystals with substantially different energy gaps (Figure 1) also argues against the formation of any specific excited state during cross relaxation. This reasoning leads us to suggest that hot *excitons* (rather than hot electrons from Mn$^{2+/3+}$ ionization) are formed by the cross-relaxation process described here.

Mn$^{2+}$ ionization energies in semiconductors are not fully understood, however, and it is conceivable that the lowest-energy Mn$^{2+/3+}$ photoionization actually occurs below the position estimated from RPES data. RPES data do show a minor peak $\sim$1 eV below the VB edge, for example, but this peak is generally assigned as a "shake-up" satellite.[51] Excited-state absorption (ESA) measurements on Mn$^{2+}$-doped ZnS and ZnSe crystals also clearly show midgap absorption from the $^{4}T_1$ state as low as $\sim$1 eV,[36,52,53] but numerous spin-allowed $d$−$d$ transitions are expected in this same energy region, and ESA is furthermore unable to distinguish between donor- and acceptor-type photoionization processes. Computational studies suggest that this ESA spectrum derives entirely from $d$−$d$ transitions.[54] Overall, the interpretation of this midgap absorption remains too tentative to draw firm conclusions about its relationship to RPES data.

The difference in PL saturation between bulk and nanocrystalline Mn$^{2+}$-doped semiconductors is also an interesting issue. Given the numerous reports of PL saturation in related phosphors,[9−11] saturation of the slow Mn$^{2+}$ PL is not unexpected, but the low excitation rates and low Mn$^{2+}$ concentrations at which it occurs in these nanocrystals appear to differentiate this saturation from those described in closely related bulk materials.[11−15] The same Mn$^{2+}$-exciton cross relaxation is undoubtedly active in bulk Mn$^{2+}$-doped semiconductors, but it is apparently not the dominant cause of saturation. In the nanocrystals investigated here, the Mn$^{2+}$ concentrations are too small for energy migration of the type observed in bulk, and time-resolved measurements reveal no slow contributions to the Mn$^{2+}$ excited-state decay dynamics. The colloidal Mn$^{2+}$-doped semiconductor nanocrystals are certainly conducive to observation of Mn$^{2+}$−exciton cross relaxation because of the absence of other nonlinear processes. Moreover, the longer intrinsic lifetimes of excitons in strongly

quantum confined nanocrystals may favor $Mn^{2+}$-exciton cross relaxation. Finally, the dominance of Auger cross relaxation may reflect enhancement of $Mn^{2+}$−exciton exchange coupling for $Mn^{2+}$ near the centers of the nanocrystals.

Beyond the interesting fundamental issues related to electronic structure, the observation of PL saturation at low CW excitation powers has important practical implications. Many excitation sources can readily reach power densities where saturation effects are not negligible ($> \sim 100$ mW/cm$^2$, Figure 1), raising the possibility that PL quantum yields or other PL properties of $Mn^{2+}$-doped semiconductors may be unknowingly measured under nonlinear conditions. Certain measurements may even be difficult to perform *without* encountering power saturation, for example, optical microscopy or single-particle spectroscopy, which often use power densities of kW/cm$^2$,[36,55] well within the saturation regime seen in Figure 1. The highly efficient cross relaxation may thus define the performance limits of these phosphors in various applications. On the positive side, the high efficiency of $Mn^{2+}$-exciton cross relaxation should provide an effective route to light-driven PL modulation, an attractive technique for improving spatial resolution in optical microscopies.[56] PL modulation via $Mn^{2+}$−exciton cross relaxation should be more effective than via midgap ESA[36] because of the much greater absorption cross section of the band-to-band transitions ($\sigma_{QD} \sim 10^{-15}$ cm$^2$ vs $\sigma_{ESA} \sim 10^{-20}$ cm$^2$).

## VI. SUMMARY

$Mn^{2+}$ PL saturation with increasing excitation power has been observed in several $Mn^{2+}$-doped semiconductor nanocrystals using low-power CW and quasi-CW photoexcitation. Two-pulse photoexcitation experiments unambiguously associate this saturation with photoexcitation of QDs that already contain $Mn^{2+}$ in its $^4T_1$ excited state. In the saturation regime, the lack of power dependence in the time-resolved excitonic PL implicates a nonradiative quenching process with kinetics similar to the exciton-to-$Mn^{2+}$ energy transfer step, which occurs with $k_{et} \sim 10^{10}$ s$^{-1}$. An Auger-type cross relaxation involving nonradiative energy transfer between an excited-state $Mn^{2+}$ and an exciton is proposed to explain the observations. A kinetic model has been developed that reproduces the experimental results using a cross-relaxation rate constant of at least $2 \times 10^{10}$ s$^{-1}$. This highly efficient cross relaxation leads to reduced PL quantum yields whenever photoexcitation rate constants are comparable to $Mn^{2+}$ decay rate constants, which are typically in the range $k_{Mn} \sim 10^3-10^4$ s$^{-1}$ ($\tau \sim 0.1-1.0$ ms). Because of the large absorption cross sections of semiconductor nanocrystals and the fast energy transfer to $Mn^{2+}$, such excitation rate constants are easily achieved. PL nonlinearities can thus be expected under many conditions, including those used for optical imaging and single-particle spectroscopies.[57,58] This highly efficient $Mn^{2+}$−exciton cross relaxation should provide an attractive alternative to $Mn^{2+}$-centered ESA for improving spatial resolution in optical microscopies via light-driven PL modulation.[56]

## ■ APPENDIX

The average diameter ($d_{avg} \equiv d_0$) of an ensemble of doped nanocrystals can be determined from the average energy of the first excitonic absorption feature. From the width and shape of this exciton absorption band, a Gaussian distribution with a standard deviation in core diameter ($\sigma$) can be estimated as given by eq A1.

$$g(d) = \frac{1}{\sqrt{2\pi}\,\sigma} e^{-(d-d_0)^2/2\sigma^2}$$
(A1)

The volume of a given particle is $V(d) = (\pi/6)d^3$ and the distribution in core volume is therefore given by eq A2, which corresponds to a skewed Gaussian.

$$g(V) = g(d)\left(\frac{\partial V}{\partial d}\right)^{-1} = g(d)\frac{2}{\pi d^2}$$
(A2)

The average number of dopants per QD of volume $V$ ($\bar{m}_v$) is proportional to the global average number of dopants per QD of average volume $V_{avg}$ ($\bar{m}$) as given by eq A3.

$$\bar{m}_v = \bar{m}\frac{V}{V_{avg}}$$
(A3)

The size distribution can thus be rewritten in terms of a dopant distribution as in eq A4.

$$g(\bar{m}_V) = g(V)\left(\frac{\partial m}{\partial V}\right)^{-1} = g(V)\frac{V_{avg}}{\bar{m}}$$
(A4)

Within each set of particles in the volume interval $[V, V + dV]$, the actual number of dopants ($m$) per QD is given by a Poisson distribution around $\bar{m}_v$, weighted by the overall number of QDs with that $\bar{m}_v$, as in eq A5.

$$g(\bar{m}_V, m) = \frac{\bar{m}_V{}^m \cdot e^{-\bar{m}_V}}{m!} \cdot g(\bar{m}_V)$$
(A5)

Figure A1 shows a two-dimensional plot with $\bar{m}_v$ in one dimension and $m$ in the other, calculated using $\bar{m} = 4.5$, $d_0 = 4.5$
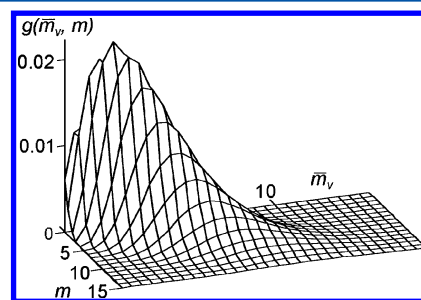


**Figure A1.** Distribution function $g(\bar{m}_v, m)$, where $\bar{m}_v$ is the average number of dopants per QD of volume $V$ and $m$ is the actual number of $Mn^{2+}$ per QD according to a Poissonian distribution around $\bar{m}_v$. This distribution function is calculated for $\bar{m} = 4.5$, $d_0 = 4.5$ nm, and $\sigma = 0.85$ nm.

nm, and $\sigma = 0.85$ nm, i.e., the parameters used for the simulations described in the manuscript text. For this plot, a Poissonian distribution was calculated for each value of $\bar{m}_v$, with an area equal to $g(\bar{m}_v)$. The distribution in Figure 5 was then generated from these data by integrating over all particles with the same number of dopants ($m$). Simulations were performed for each point along the distribution of Figure 5 with the assumption that the QD size dependence of all rate constants can be neglected.

## ■ ASSOCIATED CONTENT

**S** **Supporting Information**

Sample characterization data, parallel data for $Mn^{2+}$:ZnSe/ZnS NCs, and additional modeling results. This material is available free of charge via the Internet at http://pubs.acs.org.

## ■ AUTHOR INFORMATION

**Corresponding Author**

*Electronic address: Gamelin@chem.washington.edu.

**Notes**

The authors declare no competing financial interest.

†On sabbatical leave from the Department of Physical Chemistry, University of Geneva, 30 quai E. Ansermet, 1211 Geneva 4, Switzerland.

## ■ ACKNOWLEDGMENTS

## ■ REFERENCES

(1) Yen, W. M., Shionoya, S., Yamamoto, H., Eds. *Fundamentals of Phosphors*; CRC Press: Boca Raton, FL, 2006.

(2) Ronda, C., Ed. *Luminescence: From Theory to Applications*; Wiley-VCH: Weinheim, Germany, 2008.

(3) Vlasenko, N. A.; Popkov, Y. A. Study of Electroluminescence of a Sublimated ZnS-Mn Phosphor. *Opt. Spektrosk.* **1960**, *8*, 81.

(4) Shibata, K.; Nakayama, E.; Souma, I.; Murayama, A.; Oka, Y. Exciton Recombination Processes in $Cd_{1-x}Mn_xSe$/ZnSe Quantum Dots under Magnetic Fields. *Phys. Stat. Sol. (b)* **2002**, *229*, 473.

(5) Seufert, J.; Bacher, G.; Scheibner, M.; Forchel, A.; Lee, S.; Dobrowolska, M.; Furdyna, J. K. Dynamical Spin Response in Semimagnetic Quantum Dots. *Phys. Rev. Lett.* **2002**, *88*, 027402.

(6) Chen, H.-Y.; Chen, T.-Y.; Son, D. H. Measurement of Energy Transfer Time in Colloidal Mn-Doped Semiconductor Nanocrystals. *J. Phys. Chem. C* **2010**, *114*, 4418.

(7) Vlaskin, V. A.; Janßen, N.; van Rijssel, J.; Beaulac, R.; Gamelin, D. R. Tunable Dual Emission in Doped Semiconductor Nanocrystals. *Nano Lett.* **2010**, *10*, 3670.

(8) Beaulac, R.; Ochsenbein, S. T.; Gamelin, D. R. Colloidal Transition-Metal-Doped Quantum Dots. In *Semiconductor Quantum Dots*, 2nd ed.; Klimov, V. I., Ed. CRC Press: Boca Raton, FL, 2010; pp 397.

(9) Mikoshiba, S.; Shirai, S.; Shinada, S.; Fukushima, M. Saturation of $Zn_2SiO_4$:Mn Luminescence under Intense VUV Excitation. *J. Appl. Phys.* **1979**, *50*, 1088.

(10) de Leeuw, D. M.; 't Hooft, G. W. Method for the Analysis of Saturation Effects of Cathodoluminescence in Phosphors; Applied to $Zn_2SiO_4$:Mn and $Y_3Al_5O_{12}$:Tb. *J. Lumin.* **1983**, *28*, 275.

(11) Törnqvist, R. Manganese Concentration Dependent Saturation in ZnS:Mn Thin Film Electroluminescent Devices. *J. Appl. Phys.* **1983**, *54*, 4110.

(12) Müller, G. O.; Neugebauer, J.; Mach, R.; Reinsperger, U. Excited State Interaction in the Dopant System in ZnS:Mn Electroluminescence Devices. *J. Cryst. Growth* **1990**, *86*, 890.

(13) Vereshchagin, I. K.; Kezik, V. I.; Pautkina, A. V. Quenching of the Luminescence of ZnS:Mn at High Excitation Levels. *J. Appl. Spectrosc.* **1991**, *55*, 1175.

(14) Agekyan, V. F.; Vasil'ev, N. N.; Serov, A. Yu. Rapid Luminescence Saturation of the $Mn^{2+}$ 3d shell in the $Cd_{1-x}Mn_xTe$ Dilute Magnetic Semiconductor with a High Manganese Concentration. *Phys. Solid State* **1999**, *41*, 41.

(15) Agekyan, V. F.; Vasil'ev, N. N.; Serov, A. Yu.; Filosofov, N. G. Intracenter Luminescence of $Mn^{2+}$ in $Cd_{1-x}Mn_xTe$ and $Cd_{1-x-y}Mn_xMg_yTe$ under Intense Optical Pumping. *Phys. Solid State* **2000**, *42*, 836.

(16) Gordon, N. T.; Allen, J. W. Auger Quenching of Luminescence in ZnS:Mn. *Solid State Commun.* **1981**, *37*, 441.

(17) Gumlich, H.-E. Electro- and Photoluminescence Properties of $Mn^{2+}$ in ZnS and ZnCdS. *J. Lumin.* **1981**, *23*, 73.

(18) Langer, J. M. Where the Metal—Semiconductor Junction Emits Light. *J. Lumin.* **1981**, *23*, 141.

(19) Langer, J. M.; Lemańska-Bajorek, A.; Suchocki, A. A Method of Excitation Profiling in High-Field Electroluminescence. *Appl. Phys. Lett.* **1981**, *39*, 386.

(20) Bacher, G.; Schömig, H.; Scheibner, M.; Forchel, A.; Maksimov, A. A.; Chernenko, A. V.; Dorozhkin, P. S.; Kulakovskii, V. D.; Kennedy, T.; Reinecke, T. L. Spin—Spin Interaction in Magnetic Semiconductor Quantum Dots. *Physica E* **2005**, *26*, 37.

(21) Beaulac, R.; Archer, P. I.; Ochsenbein, S. T.; Gamelin, D. R. $Mn^{2+}$-Doped CdSe Quantum Dots: New Inorganic Materials for Spin-Electronics and Spin-Photonics. *Adv. Funct. Mater.* **2008**, *18*, 3873.

(22) Henneberger, F.; Puls, J., Diluted Magnetic Quantum Dots. In *Introduction to the Physics of Diluted Magnetic Semiconductors*; Kossut, J., Gaj, J. A., Eds.; Springer-Verlag: Berlin, 2010; Vol. 144, p 161.

(23) Besombes, L.; Léger, Y.; Maingault, L.; Ferrand, D.; Mariette, H.; Cibert, J. Probing the Spin State of a Single Magnetic Ion in an Individual Quantum Dot. *Phys. Rev. Lett.* **2004**, *93*, 207403.

(24) Besombes, L.; Léger, Y.; Maingault, L.; Mariette, H. Spin Properties of Charged Mn-Doped Quantum Dot. *J. Appl. Phys.* **2007**, *101*, 081713.

(25) Léger, Y.; Besombes, L.; Fernández-Rossier, J.; Maingault, L.; Mariette, H. Electrical Control of a Single Mn Atom in a Quantum Dot. *Phys. Rev. Lett.* **2006**, *97*, 107401.

(26) Léger, Y.; Besombes, L.; Maingault, L.; Ferrand, D.; Mariette, H. Geometrical Effects on the Optical Properties of Quantum Dots Doped with a Single Magnetic Atom. *Phys. Rev. Lett.* **2005**, *95*, 047403.

(27) Maingault, L.; Besombes, L.; Léger, Y.; Bougerol, C.; Mariette, H. Inserting One Single Mn Ion into a Quantum Dot. *Appl. Phys. Lett.* **2006**, *89*, 193109.

(28) Cerletti, V.; Coish, W. A.; Gywat, O.; Loss, D. Recipes for Spin-Based Quantum Computing. *Nanotechnology* **2005**, *16*, R27.

(29) Koenraad, P. M.; Flatté, M. E. Single Dopants in Semiconductors. *Nat. Mater.* **2011**, *10*, 91.

(30) Beaulac, R.; Schneider, L.; Archer, P. I.; Bacher, G.; Gamelin, D. R. Light-Induced Spontaneous Magnetization in Doped Colloidal Quantum Dots. *Science* **2009**, *325*, 973.

(31) Ochsenbein, S. T.; Feng, Y.; Whitaker, K. M.; Badaeva, E.; Liu, W. K.; Li, X.; Gamelin, D. R. Charge-Controlled Magnetism in Colloidal Doped Semiconductor Nanocrystals. *Nature Nanotechnol.* **2009**, *4*, 681.

(32) Beaulac, R.; Archer, P. I.; van Rijssel, J.; Meijerink, A.; Gamelin, D. R. Exciton Storage by $Mn^{2+}$ in Colloidal $Mn^{2+}$-Doped CdSe Quantum Dots. *Nano Lett.* **2008**, *8*, 2949.

(33) McLaurin, E. J.; Vlaskin, V. A.; Gamelin, D. R. Water-Soluble Dual-Emitting Nanocrystals for Ratiometric Optical Thermometry. *J. Am. Chem. Soc.* **2011**, *133*, 14978.

(34) Wang, S.; Jarrett, B. R.; Kauzlarich, S. M.; Louie, A. Y. Core/Shell Quantum Dots with High Relaxivity and Photoluminescence for Multimodality Imaging. *J. Am. Chem. Soc.* **2007**, *129*, 3848.

(35) Pradhan, N.; Battaglia, D. M.; Liu, Y.; Peng, X. Efficient, Stable, Small, and Water-Soluble Doped ZnSe Nanocrystal Emitters as Non-Cadmium Biomedical Labels. *Nano Lett.* **2007**, *7*, 312.

(36) Irvine, S. E.; Staudt, T.; Rittweger, E.; Engelhardt, J.; Hell, S. W. Direct Light-Driven Modulation of Luminescence from Mn-Doped ZnSe Quantum Dots. *Angew. Chem.* **2008**, *47*, 2685.

(37) Chen, O.; Shelby, D. E.; Yang, Y.; Zhuang, J.; Wang, T.; Niu, C.; Omenetto, N.; Cao, Y. C. Excitation-Intensity-Dependent Color-Tunable Dual Emissions from Manganese-Doped CdS/ZnS Core/Shell Nanocrystals. *Angew. Chem.* **2010**, *49*, 10132.

(38) Chen, H.-Y.; Chen, T.-Y.; Berdugo, E.; Park, Y.; Lovering, K.; Son, D. H. Hot Electrons from Consecutive Exciton-Mn Energy Transfer in Mn-Doped Semiconductor Nanocrystals. *J. Phys. Chem. C.* **2011**, *115*, 11407.

(39) Taguchi, S.; Ishizumi, A.; Kanemitsu, Y. Multicarrier Recombination and Energy Transfer in Mn-Doped CdS Nanocrystals Studied by Femtosecond Pump–Probe Spectroscopy. *J. Phys. Soc. Jpn.* **2010**, *79*, 063710.

(40) White, M. A.; Weaver, A. L.; Beaulac, R.; Gamelin, D. R. Electrochemically Controlled Auger Quenching of $Mn^{2+}$ Photoluminescence in Doped Semiconductor Nanocrystals. *ACS Nano* **2011**, *5*, 4158.

(41) Archer, P. I.; Santangelo, S. A.; Gamelin, D. R. Inorganic Cluster Syntheses of $TM^{2+}$-Doped Quantum Dots (CdSe, CdS, CdSe/CdS): Physical Property Dependence on Dopant Locale. *J. Am. Chem. Soc.* **2007**, *129*, 9808.

(42) Li, J. J.; Wang, Y. A.; Guo, W.; Keay, J. C.; Mishima, T. D.; Johnson, M. B.; Peng, X. Large-Scale Synthesis of Nearly Monodisperse CdSe/CdS Core/Shell Nanocrystals using Air-Stable Reagents via Successive Ion Layer Adsorption and Reaction. *J. Am. Chem. Soc.* **2003**, *125*, 12567.

(43) Chen, H.-S.; Lo, B.; Hwang, J.-Y.; Chang, G.-Y.; Chen, C.-M.; Tasi, S.-J.; Wang, S.-J. J. Colloidal ZnSe, ZnSe/ZnS, and ZnSe/ZnSeS Quantum Dots Synthesized from ZnO. *J. Phys. Chem. B* **2004**, *108*, 17119.

(44) Nag, A.; Chakraborty, S.; Sarma, D. D. To Dope $Mn^{2+}$ in a Semiconducting Nanocrystal. *J. Am. Chem. Soc.* **2008**, *130*, 10605.

(45) Norberg, N. S.; Parks, G. L.; Salley, G. M.; Gamelin, D. R. Giant Excitonic Zeeman Splittings in Colloidal $Co^{2+}$-Doped ZnSe Quantum Dots. *J. Am. Chem. Soc.* **2006**, *128*, 13195.

(46) Reiss, P.; Protière, M.; Li, L. Core/Shell Semiconductor Nanocrystals. *Small* **2009**, *5*, 154.

(47) Kurbanov, S. S.; Igamberdiev, K. T.; Kang, T. W. The UV-Laser Induced Heating Effect on Photoluminescence from ZnO Nanocrystals Deposited on Different Substrates. *J. Phys. D* **2010**, *43*, 115401.

(48) McGuire, J. A.; Sykora, M.; Robel, I.; Padilha, L. A.; Joo, J.; Pietryga, J. M.; Klimov, V. I. Spectroscopic Signatures of Photocharging due to Hot-Carrier Transfer in Solutions of Semiconductor Nanocrystals under Low-Intensity Ultraviolet Excitation. *ACS Nano* **2010**, *4*, 6087.

(49) Benalloul, P.; Benoit, J.; Duran, J.; Evesque, P.; Geoffroy, A. Diffusion and Trapping in ZnS:Mn Electroluminescent Thin Films. *Solid State Commun.* **1984**, *51*, 389.

(50) Taniguchi, M.; Fujimori, M.; Fujisawa, M.; Mori, T.; Souma, I.; Oka, Y. Mn 3d Partial Density-of-States and p–d Hybridization in $Cd_{1-x}Mn_xY$ (Y = S, Se and Te). *Solid State Commun.* **1987**, *62*, 431.

(51) Weidemann, R.; Gumlich, H.-E.; Kupsch, M.; Middelmann, H.-U.; Becker, U. Partial Density of Mn 3d States and Exchange-Splitting Changes in $Zn_{1-x}Mn_xY$ (Y = S,Se,Te). *Phys. Rev. B* **1992**, *45*, 1172.

(52) Dreyhsig, J.; Allen, J. W. Absorption from the Excited State in ZnS:Mn. *J. Phys.: Condens. Matter* **1989**, *1*, 1087.

(53) Dreyhsig, J.; Stutenbäumer, U.; Gumlich, H.-E.; Allen, J. W. Excited State Absorption (ESA) of Mn in ZnS and ZnSe. *J. Cryst. Growth* **1990**, *101*, 443.

(54) Stavrev, K. K.; Zerner, M. C. On the Jahn–Teller Effect on $Mn^{2+}$ in Zinc-Blende ZnS Crystal. *J. Chem. Phys.* **1995**, *102*, 34.

(55) Ebenstein, Y.; Mokari, T.; Banin, U. Fluorescence Quantum Yield of CdSe/ZnS Nanocrystals Investigated by Correlated Atomic-Force and Single-Particle Fluorescence Microscopy. *Appl. Phys. Lett.* **2002**, *80*, 4033.

(56) Gustafsson, M. G. L. Nonlinear Structured-Illumination Microscopy: Wide-Field Fluorescence Imaging with Theoretically Unlimited Resolution. *Proc. Natl. Acad. Sci. U.S.A.* **2005**, *102*, 13081.

(57) Zhang, Y.; Gan, C.; Muhammad, J.; Battaglia, D.; Peng, X.; Xiao, M. Enhanced Fluorescence Intermittency in Mn-Doped Single ZnSe Quantum Dots. *J. Phys. Chem. C* **2008**, *112*, 20200.

(58) Ishizumi, A.; Kanemitsu, Y. Blinking Behavior of Surface-Defect and Impurity Luminescence in Nondoped and $Mn^{2+}$-Doped CdS Nanocrystals. *J. Phys. Soc. Jpn.* **2009**, *78*, 083705.